High-working-pressure Sputtering of ZnO for Stable and Efficient Perovskite Solar Cells

Il Jeon, Abhishek Thote, Hao-Sheng Lin, Sergei Manzhos, Takafumi Nakagawa, Donguk Suh, Junho Hwang, Makoto Kashiwagi, Junichiro Shiomi, Shigeo Maruyama, Hirofumi Daiguji* and Yutaka Matsuo**

Dr. I. Jeon, A. Thote, H.-S Lin, Dr. Manzhos, Dr. T. Nakagawa, Dr. D. Suh, Dr. J. Hwang, Dr. M. Kashiwagi, Prof. J. Shiomi, Prof. S. Maruyama, Prof. H. Daiguji, Prof. Y. Matsuo
Department of Mechanical Engineering, The University of Tokyo 7-3-1 Hongo, Bunkyo-ku, Tokyo 113-8656, Japan
E-mail: maruyama@photon.t.u-tokyo.ac.jp, daiguji@thml.t.u-tokyo.ac.jp, matsuo@photon.t.u-tokyo.ac.jp

Dr. Sergei Manzhos
Department of Mechanical Engineering, National University of Singapore,
Block EA #07-08, 9 Engineering Drive 1, Singapore 117576, Singapore

Prof. S. Maruyama
Research Institute for Energy Conservation, National Institute of Advanced Industrial Science and Technology, Tsukuba 305-8565, Japan

Prof. Y. Matsuo
Hefei National Laboratory for Physical Sciences at the Microscale, University of Science and Technology of China, Hefei, Anhui 230026, China

Keywords: perovskite solar cells, ZnO, sputtering, perovskite degradation, high working pressure

Owing to its high mobility with a low sintering temperature, ZnO is a promising electron-transporting material for flexible and tandem applications of perovskite solar cells. However, ZnO inevitably triggers the degradation of perovskite materials. Such degradation can be inhibited when ZnO films with good stoichiometry and minimum interstitials are used. In this work, a record-high efficiency with substantial stability of ZnO-based perovskite solar cells is obtained using a high-working-pressure-sputtering technique. The high-working-pressure-sputtering process can produce higher quality ZnO films with fewer surface defects compared with conventional sputtering and sol-gel ZnO solution process. A power conversion efficiency of 17.3% was obtained, which is the highest among the values reported for single compact ZnO layer-based perovskite solar cells. In addition, the stability of these devices was significantly higher than that of the conventional ZnO-based perovskite solar cells. This

indicates that ZnO can be a good candidate for the electron-transporting layer in perovskite solar cells, especially for flexible and tandem applications.

The photovoltaic community has witnessed a rapid development of perovskite solar cells (PSCs) in recent years, because of their high power conversion efficiency (PCE) while retaining the advantages of thin-film solar cells. As much as the organometallic halide perovskite light-absorbers of PSCs are important, the charge-transporting layers play an equally vital role.[1] ZnO electron transporting layer (ETL) in PSCs has been investigated by many researchers as an alternative to the widely used TiO_2.[2–5] This is because ZnO requires a low sintering temperature, which is a prerequisite for printability on flexible substrates.[6-8] Moreover, ZnO has electron mobilities between 200 and 300 cm^2 V s^{-1}, which are approximately one order of magnitude higher than those of TiO_2.[9–11] However, ZnO in PSCs has not been preferred over TiO_2 in PSCs because it leads to a faster degradation of the perovskite layer.[3,12,13] It was observed that residual chemicals,[14,15] adsorbed water molecules,[16,17] ZnO interstitials,[18,19] and the basicity of ZnO[20–22] contribute to the degradation. To avoid this problem, several solutions, such as adding a layer on top of ZnO,[14,23,24] doping with Al,[25,26] and a two-step deposition method, have been proposed thus far.[8,27] Nevertheless, these methods require more fabrication steps, which is not ideal for achieving a facile PSC process.[28] Amongst the proposed solutions, a sputtering process of ZnO is deemed the most promising, and has already been demonstrated by number of researchers.[29–31] Contrary to the general perception, ZnO sputtering does not increase the fabrication cost, because it is an extention of the indium tin oxide (ITO) deposition, which is also a sputtering process.[32] Furthermore, sputtering does not require stabilizing ligands, which exacerbate the degradation of perovskite layer.[14,15] However, sputtered ZnO still contains interstitial defects on its surface, which leads to the formation of hydroxyl groups, triggering the degradation of the perovskite layer.[33–35]

Previously, we reported a novel sputtering method for generating ZnO films with high conductivity and crystallinity by controlling the working pressure inside the sputter chamber.[32] High working pressure (HWP) during the sputtering reduced the energy of the high-energy particles, such as Ar, by controlling the bombardment energy, resulting in reduced recombination centers. This produced ZnO films with more balanced Zn to O stoichiometry with fewer defects (**Figure S1**). Organic solar cells fabricated on this HWP-sputtered ZnO showed a significant increase in device performance. In this work, we used HWP-sputtered ZnO films in PSCs and demonstrated that they improved both the efficiency and stability significantly. This communication reveals that the HWP-sputtering also improves the surface properties of ZnO which have a direct impact on the stability of the perovskite material on top. Ultimately, a PCE of 17.3%, which is the highest efficiency among the reported values for single compact ZnO ETL-based PSCs, was obtained from the HWP-sputtered ZnO-based PSCs with high stability.

The faster perovskite degradation on ZnO is due to the intrinsic surface properties of ZnO. There are two ways to be discussed in this regard. The first aspect is the degradation through moisture, which is accelerated in the presence of ZnO. It is well known that $CH_3NH_3PbI_3$ ($MAPbI_3$) dissociates into CH_3NH_3I and PbI_2 by water (1).[16] CH_3NH_3I can further decompose into CH_3NH_2 and HI (2).[22] Unlike TiO_2, ZnO reacts with HI to produce ZnI_2 and H_2O, and consequently, the degradation is accelerated (3).[36] The second aspect is the defect sites on the surface of ZnO. CH_3NH_3I terminations on the surface of the perovskite films interact with ZnO chiefly by forming I-Zn bonds if there are uncoordinated Zn defect sites. The deprotonation can result in methylammonium ($CH_3NH_3^+$) next to Zn producing methylamine (CH_3NH_2) with the released protons being absorbed by vicinal oxygen.[13] This is not observed in the case of perovskite on TiO_2.[37] These uncoordinated Zn and Zn interstitials lead to the formation of hydroxyl groups and $Zn(OH)_2$ species, which can react

with CH_3NH_3I to etch the ZnO film (4).[38] Therefore, it is imperative that ZnO be free from both water and surface defects.

$$CH_3NH_3PbI_3 \rightleftharpoons CH_3NH_3I + PbI_2 \quad (1)$$

$$CH_3NH_3I \rightleftharpoons CH_3NH_2 + HI \quad (2)$$

$$ZnO + 2HI \rightleftharpoons ZnI_2 + H_2O \quad (3)$$

$$Zn(OH)_2 + 4CH_3NH_2 \cdot HI \rightarrow [Zn(CH_3NH_2 \cdot HI)_4]^{2+} + 2OH^- \quad (4)$$

As it is important to prevent the initiation of the perovskite degradation in ZnO-based PSCs, all the processes were performed inside a glove box. Further, all ZnO films were pre-annealed for 10 min before the perovskite deposition to dry off even trace amounts of water molecules.[17] Such pre-annealing of ZnO was crucial in obtaining high PCEs (**Table S1**). The annealing of the perovskite was limited to 10 min to prevent the triggering of perovskite degradation by the polar dimethylformamide (DMF) solvent. 10 min was enough to obtain perovskite grains of sufficient size as ZnO induces a faster growth of perovskite crystals via the formation of a tetragonal phase.[39–41] We prepared four different types of ZnO ETL films: two splits of sol-gel ZnO films annealed at 300 °C and 500 °C, sputtered ZnO films, and HWP-sputtered ZnO films (**Figure 1a**). The HWP-sputter process is briefly illustrated in **Figure 1b**. We assessed the accelerated degradation by depositing $CH_3NH_3PbI_3$ on these films and annealed them at 105 °C in air (**Figure 1c**). It was apparent even with the naked eye that the sol-gel ZnO at 300 °C showed the lowest stability and the HWP-sputtered ZnO showed the highest stability (**Figure 1d**). The instability of sol-gel ZnO was due to the high concentration of hydroxyl and acetate groups produced via the hydrolysis reaction.[12–15] The sol-gel ZnO annealed at 500 °C was relatively more stable than the sol-gel ZnO annealed at 300 °C owing to evaporation of aminoethan-1-ol ligands as demonstrated using energy-

dispersive X-ray analysis (EDX) and X-ray photoelectron spectroscopy (XPS) (**Figure S2 and S3**). ZnO annealed at 500 °C shows reduced carbon and nitrogen amounts according to EDX, which indicate the reduced amount of aminoethan-1-ol (**Figure S2**). XPS also shows that the carbon intensity decreased for the ZnO samples annealed at 500 °C, corroborating our hypothesis (**Figure S3a**). The stability difference between sputtered ZnO and HWP-sputtered ZnO was visibly unclear, hence UV-vis spectroscopy was used to differentiate them (**Figure 1e and f**). It is evident from the data that the absorption of $CH_3NH_3PbI_3$ on sputtered ZnO was reduced after aging for 1h (**Figure 1e**), whereas the absorption of $CH_3NH_3PbI_3$ on HWP-sputtered ZnO did not change for 1 h (**figure 1f**).

Understanding the stability difference between the sputtered ZnO and the HWP-sputtered ZnO is much more challenging. Therefore, detailed investigation of the interface of ZnO is necessary. As mentioned above, more surface interstitials caused by unbalanced stoichiometry can lead to a faster degradation of perovskite. XPS oxygen peaks (**Figure S3b**) and Zn peaks (**Figure S3c**) confirm that HWP-sputtered ZnO possesses fewer Zn defects and oxygen-deficient species than the sputtered ZnO, which is consistent with our previous finding.[32] **Figure S3b** shows that the oxygen-deficient shoulder, which represents interstitial sites, is much smaller for the HWP-sputtered ZnO. In addition, Zn peaks for the HWP sputtered ZnO films are shifted to a lower binding energy, which indicates that more Zn is bonded to oxygen, indicating fewer interstitials at the interface. To support this, we performed photoelectron yield spectroscopy (PYS) measurement for the HWP-sputtered ZnO and sputtered ZnO films. The data denotes that the HWP-sputtered ZnO films possess a higher valence level by approximately 0.3 eV compared with the sputtered ZnO films (**Figure S4**). We observe that the two films have different surface properties. This indicates that HWP-sputtered ZnO possesses fewer interstitials than conventionally sputtered ZnO as the oxygen non-stoichiometry is reported to downshift the valence edge.[42-44]

To enhance the observation of the interface properties of ZnO, we analyzed the ZnO surface before and after the interaction of ZnO with $MAPbI_3$ (**Figure 2a**). By depositing and degrading $MAPbI_3$ on ZnO, and therefter washing it off using DMF, we could induce a greater difference between HWP-sputtered ZnO and sputtered ZnO (convention) surfaces. Water contact angle test, Fourier-transform infrared spectroscopy (FTIR), and XPS were used to observe the difference before and after the interaction. Water contact angle data show that sputtered ZnO is more hydrophilic than HWP-sputtered ZnO before the deposition of $MAPbI_3$ (**Figure 2b**). The difference in the water contact angle increases after the interaction, as both films become more hydrophilic. This can be explained by surface condition of ZnO. As more charged species on the ZnO surfaces attract polar water molecules via ionic interaction, sputtered ZnO with more defect sites such as Zn^{2+} and non-stoichiometric OH will be more hydrophilic than HWP-sputtered ZnO. The increased hydrophilicity of the films become more hydrophilic after the deposition and degradation of $MAPbI_3$ indicates that there are more charged species are generated from the interaction between ZnO and $MAPbI_3$. This can be explained by equations (3) and (4), according to which ZnI_2, $Zn(OH)_x$, and $[Zn(CH_3NH_2 \cdot HI)_4]^{2+}$ are generated on the ZnO surface when $MAPbI_3$ degrades.[13] The sputtered ZnO became even more hydrophilic than HWP-sputtered ZnO after washing off $MAPbI_3$ because more charged species were generated, corroborating our hypothesis that HWP-sputtered ZnO possesses a better interface, leading to slower degradation. Transmission FTIR analysis provided chemical evidence of this phenomenon. Both sputtered ZnO and HWP-sputtered ZnO on Si substrates have Zn–O peaks at 450 cm^{-1}, and $Zn(OH)_2$ peaks at 600 cm^{-1} with similar intensities (**Figure 2c**).[40,45,46] After depositing and washing off $MAPbI_3$, both Zn–O and $Zn(OH)_2$ peaks of the sputtered ZnO became stronger, indicating that more Zn interstitials and hydroxyl groups were generated on its surface. Moreover, the peak corresponding to the Si–O peak from the Si substrates at 1050 cm^{-1} intensified for the sputtered ZnO. Considering that the peak of the Si substrate should possess the same intensity

of its peak, we suspected that this peak may indicate the generation of Zn–I. Nonetheless, the FTIR peak of Zn–I has not been reported yet and cannot be found on the FTIR database to the best of our knowledge. Therefore, we performed powder FTIR of ZnI_2(s) to identify the Zn–I peak. **Figure S5** shows that there is a strong peak at 1050 cm^{-1} without Si substrates and small peaks around 900 cm^{-1} and 1400 cm^{-1}. This indicates that the strong enhancement of the peak at 1050 cm^{-1} is due to the generation of Zn–I. In addition, a set of weak peaks appeared near 1400 cm^{-1} for both sputtered and HWP-sputtered ZnO. Peaks in this region can be attributed C–H, N–H, O–H, and even Zn–I. The peaks may originate from $Zn(OH)_x$ and $[Zn(CH_3NH_2 \cdot HI)_4]^{2+}$ species. These small peaks for the sputtered ZnO were stronger than those of HWP-sputtered ZnO.

XPS was used to investigate the ZnO interface further. **Figure S6** shows $2P_{3/2}$ peaks of sputtered ZnO and HWP-sputtered ZnO at a high resolution after calibrating their binding energies for comparison. We can observe that the sputtered ZnO $2P_{3/2}$ peak was slightly broader and with a higher binding energy. This indicates the existence of Zn species bonded to hydroxides.[47] **Figure 3a and b** show $2P_{3/2}$ Zn peaks before and after the interaction with $MAPbI_3$. We can observe that, in both sputtered ZnO and HWP-sputtered ZnO, the Zn peaks decreased significantly. We suspect that the etching of Zn during the interaction with $MAPbI_3$ may have etched off ZnO which is less than 20 nm thick. However, the peak positions were different. The peak of sputtered ZnO (**Figure 3a**) was shifted to a slightly lower binding energy than that of HWP-sputtered ZnO (**Figure 3b**). This can be attributed to the fact that more $[Zn(CH_3NH_2 \cdot HI)_4]^{2+}$ complexes are formed for the sputtered ZnO due to the greater number of intrinsic defect sites (4). However, for the HWP-sputtered ZnO, there are more ZnI (3), because of fewer defect sites. 1s O XPS peaks also point to the same conclusion (**Figure 3c and d**). Before the deposition of $MAPbI_3$, sputtered ZnO shows a stronger oxygen-deficient component of the oxygen peak (**Figure 3c**) than that of HWP-sputtered ZnO (**Figure**

3d) (**Figure S7**). After depositing $MAPbI_3$ and washing it off with DMF, the oxygen-deficient component was enhanced in both the ZnO samples. However, the oxygen-deficient component was again much stronger for the sputtered ZnO sample (**Figure 3c**) than that of the HWP-sputtered ZnO sample (**Figure 3d**). The interaction between ZnO and $MAPbI_3$ is summarized and graphically depicted in **Figure 3e**. The actual effect of the difference between the two types of sputtered ZnO films can be observed using photoluminescence (PL). PL data in **Figure S8** show that the perovskite on HWP-sputtered ZnO became quenched more than that on sputtered ZnO. In addition, HWP-sputtered ZnO PL spectrum is slightly blue shifted (~7 nm) with a narrower full width at half maximum (FWHM). The blue shift denotes passivation of the trap states on the perovskite surface as they lead to spontaneous radiative recombination at the surface.[48] Moreover, the narrower FWHM indicates a reduction in shallow trap density at the interface between HWP-sputtered ZnO and the perovskite, revealing that there are fewer defects at the HWP-sputtered ZnO interface.[49] The perovskite films on ZnO were studied using scanning electron microscopy (SEM). According to the SEM images in **Figure S9**, The films of $MAPbI_3$ on sol-gel ZnO were of poor quality films with many voids, among which the samples annealed at 500 °C appeared slightly better (**Figure S9a and b**). The $MAPbI_3$ films on sputtered ZnO exhibited high film quality and were free of voids; the grain size of the perovskite on HWP-sputtered ZnO was marginally larger than the that on sputtered ZnO (**Figure S9c and d**). This can be ascribed to the hydrophobicity of HWP-sputtered ZnO (**Figure 2b**) as a more hydrophobic substrate results in larger grain size.[50]

After investigating the surface properties of the different ZnO films, we fabricated PSCs using these ZnO films and measured their photovoltaic performances (**Table S2**). As expected, the sol-gel ZnO-based PSCs exhibited much lower PCEs than the sputtered ZnO-based PSCs, although the sol-gel ZnO annealed at 500 °C exhibited higher PCEs than that

annealed at 300 °C. The HWP-sputtered ZnO ETL-based PSCs exhibited a much higher PCE of 17.3% than the sputtered ZnO ETL-based PSCs (15.2%) (**Figure 4a, b, c, d, and e**). Overall, the increases in all of the three photovoltaic parameters enhanced the PCE. The higher short-circuit current density (J_{SC}) was due to larger grain size (**Figure 4a**). The higher fill factor (FF) was due to the higher conductivity owing to better oxygen stoichiometry (**Figure 4c**).[51–53] The slight increase in open-circuit voltage (V_{OC}) was probably due to the difference in ZnO interstitials[18] and surface trap sites[54] (**Figure 4b**). This is also linked to the lower hysteresis of the HWP-sputtered ZnO ETL-based PSCs (**Table S2**).[55] Moreover, the stability of the encapsulated HWP-sputtered ZnO ETL-based PSCs in air was much higher than that of the sputtered ZnO ETL-based PSCs in the same condition (**Figure 4f**). The outcomes are reasonable considering the difference between surface properties of the two types of sputtered ZnO samples. The HWP-sputtered ZnO does not trigger the perovskite degradation as fast as the sputtered ZnO. The PCE of 17.3% obtained for the HWP-sputtered ZnO ETL-based PSC is the highest among the reported PCEs for single compact ZnO ETL-based PSCs (**Figure 4g**).[8]

In conclusion, ZnO films produced via a HWP sputtering process had good stoichiometry and minimum defects. Accordingly, high-performance and stable ZnO-based PSCs were realized. The surface property of the ZnO films was analyzed from various perspectives. In addtion, the relationship between the surface property and the device performance was investigated by examining the interaction between ZnO and $MAPbI_3$ during the degradation. As the sputtering process is used for the deposition of indium tin oxide electrode, the sputtering of ZnO is as effective as the solution process in terms of the fabrication cost and large-size application. In fact, as evidenced by our work, HWP-sputtered ZnO can be used to produce high-performance and highly stable ZnO ETL-based PSCs. As ZnO plays a vital role in the tandem application of PSCs, our next step in this research is to

apply HWP sputtering to silicon-perovskite tandem solar cells.

Experimental Section

ZnO preparation: Patterned indium-doped tin oxide substrates of dimensions 15 × 15 mm (Techno Print Co. Ltd., ~ 9 Ω $sq.^{-1}$) were used for the experiments. They were sequentially cleaned with water, acetone, and 2-isopropanol for 15 min each, and subsequently subjected to UV/O_3 treatment for 15 min. For sol-gel ZnO, a 0.1 M solution of zinc acetate dihydrate ($Zn(CH_3COO)_2 \cdot 2H_2O$) (Wako, 99.0%) in ethanol (Wako, 99.5%) was prepared and subsequently subjected to rigorous stirring for 2–3 h at 80 °C. Subsequently, an ethanolamine stabilizer (28% in weight) was added and the solution was stirred for further 12–15 h at 60 °C. Radio frequency (RF) magnetron sputtering was employed to obtain both conventionally sputtered ZnO and HWP-sputtered ZnO. ZnO_x ceramic target obtained from Kojundo Chemical Laboratory Co., Ltd was used for sputtering. The RF power used for the deposition process was 100 W. The sputter deposition time was varied proportionately for the sputtered and HWP-sputtered films to obtain a similar thickness. The deposition was performed in an environment of Ar and O_2, where O_2 partial pressure was maintained at 1% of the pressure of the gas mixture. The normal sputter deposition was performed at a pressure of 2.6×10^{-1} Pa, whereas the HWP sputtering was performed at a pressure of 2.6×10^{0} Pa.

Device Fabrication: The photoactive layer of $MAPbI_3$ is prepared using a 1:1:1 molar mixture of MAI (TCI), PbI_2 (TCI), and dimethyl sulfoxide (DMSO) (Sigma Aldrich) at 50 wt% in a nitrogen environment. The mixture was stirred without heating and left for complete dissolution. Subsequently, 50 µL of this solution was spin-coated on pre-annealed ZnO thin films at 4000 rpm for 30 s. Further, 0.1 mL of diethyl ether was deposited 7.5 s after the spin-coating process was initiated. The $CH_3NH_3I.PbI_2$.DMSO adduct film was annealing on a hot plate at 100 °C for 10 min to obtain a brown-colored perovskite thin film. To prepare the hole

transport material solution, 80 mg spiro-MeOTAD, 15 μL stock solution of lithium bis(trifluoromethylsulphonyl)imide in acetonitrile (520 mg mL^{-1}), and 22.5 μL 4-tert-butylpyridine were dissolved in 1 mL chlorobenzene. Subsequently, 15 μL of this solution was spin-coated on the perovskite layer to form the hole transport layer. Finally, ~50-nm-thick gold electrodes were deposited on the substrates via thermal evaporation in vacuum.

Characterizations: The *J–V* characteristics were measured using a software-controlled source meter (Keithley 2400 SourceMeter) under dark conditions and the simulated sunlight irradiation of 1 sun (AM 1.5G; 100 mW cm^{-2}) using a solar simulator (EMS-35AAA, Ushio Spax Inc.) with a Ushio Xe short arc lamp 500. The source meter was calibrated using a silicon diode (BS-520BK, Bunkokeiki). SEM analysis of the perovskite films was performed using an S-4800 (Hitachi). The SEM and EDX measurements of ZnO films were performed using JSM-7001F (JEOL) and JED-2300F (JEOL), respectively. Shimazu UV-3150 was used for the UV–vis–NIR measurement. The PL measurements were performed using JASCO Spectrofluorometer (FP-8300). The valence band and Fermi levels measurements of ZnO films were performed using Riken Keiki PYS-A AC-2 and Kelvin probe spectroscopy in air (ESA), respectively. The photoemission measurements were performed using XPS (PHI5000, Versa Probe) with monochromatic Al Kα radiation. The water contact angle measurements were performed using a contact angle meter (DMo-501, Kyowa Interface Science Co., Ltd.). The substrates were annealed on a hot plate at 110 °C for 10 min before performing water contact angle measurements to evaporate the deposited vapors on the films. Transmission FTIR measurements were performed using Shimazu IRAffinity-1S.

Supporting Information

Supporting Information is available from the Wiley Online Library or from the author.

Acknowledgements

I.J and A.T contributed equally to this work. We gratefully acknowledge the Research and Education Consortium for Innovation of Advanced Integrated Science by Japan Science and Technology (JST) and Japan Society for the Promotion of Science (JSPS) KAKENHI Grant Numbers JP15H05760, JP16H02285, 17K04970, and 17H06609.

Received: ((will be filled in by the editorial staff))
Revised: ((will be filled in by the editorial staff))
Published online: ((will be filled in by the editorial staff))

References

[1] Z. Yu, L. Sun, *Adv. Energy Mater.* **2015**, *5*, 1500213.

[2] D.-Y. Son, J.-H. Im, H.-S. Kim, N.-G. Park, *J. Phys. Chem. C* **2014**, *118*, 16567–16573.

[3] D. Bi, G. Boschloo, S. Schwarzmüller, L. Yang, E. M. J. Johansson, A. Hagfeldt, *Nanoscale* **2013**, *5*, 11686.

[4] D. Liu, T. L. Kelly, *Nat. Photonics* **2013**, *8*, 133–138.

[5] J. You, L. Meng, T.-B. Song, T.-F. Guo, Y. (Michael) Yang, W.-H. Chang, Z. Hong, H. Chen, H. Zhou, Q. Chen et al., *Nat. Nanotechnol.* **2015**, *11*, 75–81.

[6] J. Burschka, N. Pellet, S.-J. Moon, R. Humphry-Baker, P. Gao, M. K. Nazeeruddin, M. Grätzel, *Nature* **2013**, *499*, 316–319.

[7] M. M. Lee, J. Teuscher, T. Miyasaka, T. N. Murakami, H. J. Snaith, *Science* **2012**, *338*, 643–647.

[8] P. Zhang, J. Wu, T. Zhang, Y. Wang, D. Liu, H. Chen, L. Ji, C. Liu, W. Ahmad, Z. D. Chen et al., *Adv. Mater.* **2018**, *30*, 1703737.

[9] A. K. Chandiran, M. Abdi-Jalebi, M. K. Nazeeruddin, M. Grätzel, *ACS Nano* **2014**, *8*, 2261–2268.

[10] Ü. Özgür, Y. I. Alivov, C. Liu, A. Teke, M. A. Reshchikov, S. Doğan, V. Avrutin, S.-J. Cho, H. Morkoç, *J. Appl. Phys.* **2005**, *98*, 41301.

[11] P. Ivanoff Reyes, C.-J. Ku, Z. Duan, Y. Xu, E. Garfunkel, Y. Lu, *Appl. Phys. Lett.* **2012**, *101*, 31118.

[12] D. Liu, J. Yang, T. L. Kelly, *J. Am. Chem. Soc.* **2014**, *136*, 17116–17122.

[13] J. Yang, B. D. Siempelkamp, E. Mosconi, F. De Angelis, T. L. Kelly, *Chem. Mater.* **2015**, *27*, 4229–4236.

[14] Y. Cheng, Q.-D. Yang, J. Xiao, Q. Xue, H.-W. Li, Z. Guan, H.-L. Yip, S.-W. Tsang, *ACS Appl. Mater. Interfaces* **2015**, *7*, 19986–19993.

[15] Y. Guo, X. Li, L. L. Kang, X. He, Z. Q. Ren, J. D. Wu, J. Y. Qi, *RSC Adv.* **2016**, *6*, 62522–62528.

[16] J. M. Frost, K. T. Butler, F. Brivio, C. H. Hendon, M. van Schilfgaarde, A. Walsh, *Nano Lett.* **2014**, *14*, 2584–2590.

[17] Y. Dkhissi, S. Meyer, D. Chen, H. C. Weerasinghe, L. Spiccia, Y.-B. Cheng, R. A. Caruso, *ChemSusChem* **2016**, *9*, 687–695.

[18] I. Il Jeon, S. Zeljkovic, K. Kondo, M. Yoshizawa, Y. Matsuo, *ACS Appl. Mater. Interfaces* **2016**, *8*, 29866–29871.

[19] N. Aristidou, C. Eames, I. Sanchez-Molina, X. Bu, J. Kosco, M. S. Islam, S. A. Haque, *Nat. Commun.* **2017**, *8*, 15218.

[20] M. Yang, G. Pang, J. Li, L. Jiang, D. Liang, S. Feng, *J. Phys. Chem. C* **2007**, *111*, 17213–17220.

[21] M. Kosmulski, *Chemical Properties of Material Surfaces*, CRC Press, **2001**.

[22] G. Niu, W. Li, F. Meng, L. Wang, H. Dong, Y. Qiu, *J. Mater. Chem. A* **2014**, *2*, 705–710.

[23] J. Kim, G. Kim, T. K. Kim, S. Kwon, H. Back, J. Lee, S. H. Lee, H. Kang, K. Lee, *J. Mater. Chem. A* **2014**, *2*, 17291–17296.

[24] L. Zuo, Z. Gu, T. Ye, W. Fu, G. Wu, H. Li, H. Chen, *J. Am. Chem. Soc.* **2015**, *137*, 2674–2679.

[25] J. Dong, Y. Zhao, J. Shi, H. Wei, J. Xiao, X. Xu, J. Luo, J. Xu, D. Li, Y. Luo et al., *Chem. Commun.* **2014**, *50*, 13381–13384.

[26] X. Zhao, H. Shen, Y. Zhang, X. Li, X. Zhao, M. Tai, J. Li, J. Li, X. Li, H. Lin, *ACS Appl. Mater. Interfaces* **2016**, *8*, 7826–7833.

[27] J. Song, J. Bian, E. Zheng, X.-F. Wang, W. Tian, T. Miyasaka, *Chem. Lett.* **2015**, *44*, 610–612.

[28] G. E. Eperon, T. Leijtens, K. A. Bush, R. Prasanna, T. Green, J. T.-W. Wang, D. P. McMeekin, G. Volonakis, R. L. Milot, R. May et al., *Science* **2016**, *354*, 861–865.

[29] Z.-L. Tseng, C.-H. Chiang, C.-G. Wu, *Sci. Rep.* **2015**, *5*, 13211.

[30] L. Liang, Z. Huang, L. Cai, W. Chen, B. Wang, K. Chen, H. Bai, Q. Tian, B. Fan, *ACS Appl. Mater. Interfaces* **2014**, *6*, 20585–20589.

[31] W. Lai, K. Lin, T. Guo, P. Chen, Y. Wang, *Appl. Phys. Lett.* **2015**, *107*, 253301.

[32] I. Jeon, Y. Qian, S. Nakao, D. Ogawa, R. Xiang, T. Inoue, S. Chiashi, T. Hasegawa, S. Maruyama, Y. Matsuo, *J. Mater. Chem. A* **2016**, *4*, 18763–18768.

[33] H. Li, J.-L. Bredas, *Adv. Mater.* **2016**, *28*, 3928–3936.

[34] G. Kresse, O. Dulub, U. Diebold, *Phys. Rev. B* **2003**, *68*, 245409.

[35] H. Li, L. K. Schirra, J. Shim, H. Cheun, B. Kippelen, O. L. A. Monti, J.-L. Bredas, *Chem. Mater.* **2012**, *24*, 3044–3055.

[36] H. Kanno, J. Hiraishi, *J. Raman Spectrosc.* **1980**, *9*, 85–89.

[37] E. Mosconi, E. Ronca, F. De Angelis, *J. Phys. Chem. Lett.* **2014**, *5*, 2619–2625.

[38] F. Yang, D.-W. Kang, Y.-S. Kim, *RSC Adv.* **2017**, *7*, 19030–19038.

[39] T. Baikie, Y. Fang, J. M. Kadro, M. Schreyer, F. Wei, S. G. Mhaisalkar, M. Graetzel, T. J. White, *J. Mater. Chem. A* **2013**, *1*, 5628.

[40] J. Zhang, E. J. Juárez-Pérez, I. Mora-Seró, B. Viana, T. Pauporté, *J. Mater. Chem. A* **2015**, *3*, 4909–4915.

[41] A. Bera, A. D. Sheikh, M. A. Haque, R. Bose, E. Alarousu, O. F. Mohammed, T. Wu, *ACS Appl. Mater. Interfaces* **2015**, *7*, 28404–28411.

[42] Q. Bao, X. Liu, Y. Xia, F. Gao, L.-D. Kauffmann, O. Margeat, J. Ackermann, M. Fahlman, *J. Mater. Chem. A* **2014**, *2*, 17676–17682.

[43] P. Erhart, K. Albe, A. Klein, *Phys. Rev. B* **2006**, *73*, 205203.

[44] A. Janotti, C. G. V. D. Walle, *Phys. Rev. B* **2007**, *76*, 165202.

[45] M. F. Parveen, S. Umapathy, V. Dhanalakshmi, R. Anbarasan, *Compos. Interfaces* **2010**, *17*, 757–774.

[46] F. Zhu, D. Persson, D. Thierry, C. Taxen, *CORROSION* **2000**, *56*, 1256–1265.

[47] S. Dhara, K. Imakita, P. K. Giri, M. Mizuhata, M. Fujii, *Appl. Phys. Lett.* **2013**, *114*, 134307.

[48] Y. Shao, Z. Xiao, C. Bi, Y. Yuan, J. Huang, *Nat. Commun.* **2014**, *5*, 5784.

[49] D. W. de Quilettes, S. M. Vorpahl, S. D. Stranks, H. Nagaoka, G. E. Eperon, M. E. Ziffer, H. J. Snaith, D. S. Ginger, *Science* **2015**, *348*, 683–686.

[50] C. Bi, Q. Wang, Y. Shao, Y. Yuan, Z. Xiao, J. Huang, *Nat. Comnun.* **2015**, *6*, 7747.

[51] Y. Wang, J. Zhao, S. Zhang, Q. Liu, X. Wu, *J. Non. Cryst. Solids* **2005**, *351*, 1477–1480.

[52] R. Martins, E. Fortunato, P. Nunes, I. Ferreira, A. Marques, M. Bender, N. Katsarakis, V. Cimalla, G. Kiriakidis, *J. Appl. Phys.* **2004**, *96*, 1398–1408.

[53] I. V. Tudose, P. Horváth, M. Suchea, S. Christoulakis, T. Kitsopoulos, G. Kiriakidis, *Appl. Phys. A* **2007**, *89*, 57–61.

[54] M. A. Mahmud, N. K. Elumalai, M. B. Upama, D. Wang, K. H. Chan, M. Wright, C. Xu, F. Haque, A. Uddin, *Sol. Energy Mater. Sol. Cells* **2017**, *159*, 251–264.

[55] N. Ahn, I. Jeon, J. Yoon, E. I. Kauppinen, Y. Matsuo, S. Maruyama, M. Choi, *J. Mater. Chem. A* **2018**, *6*, 1382–1389.

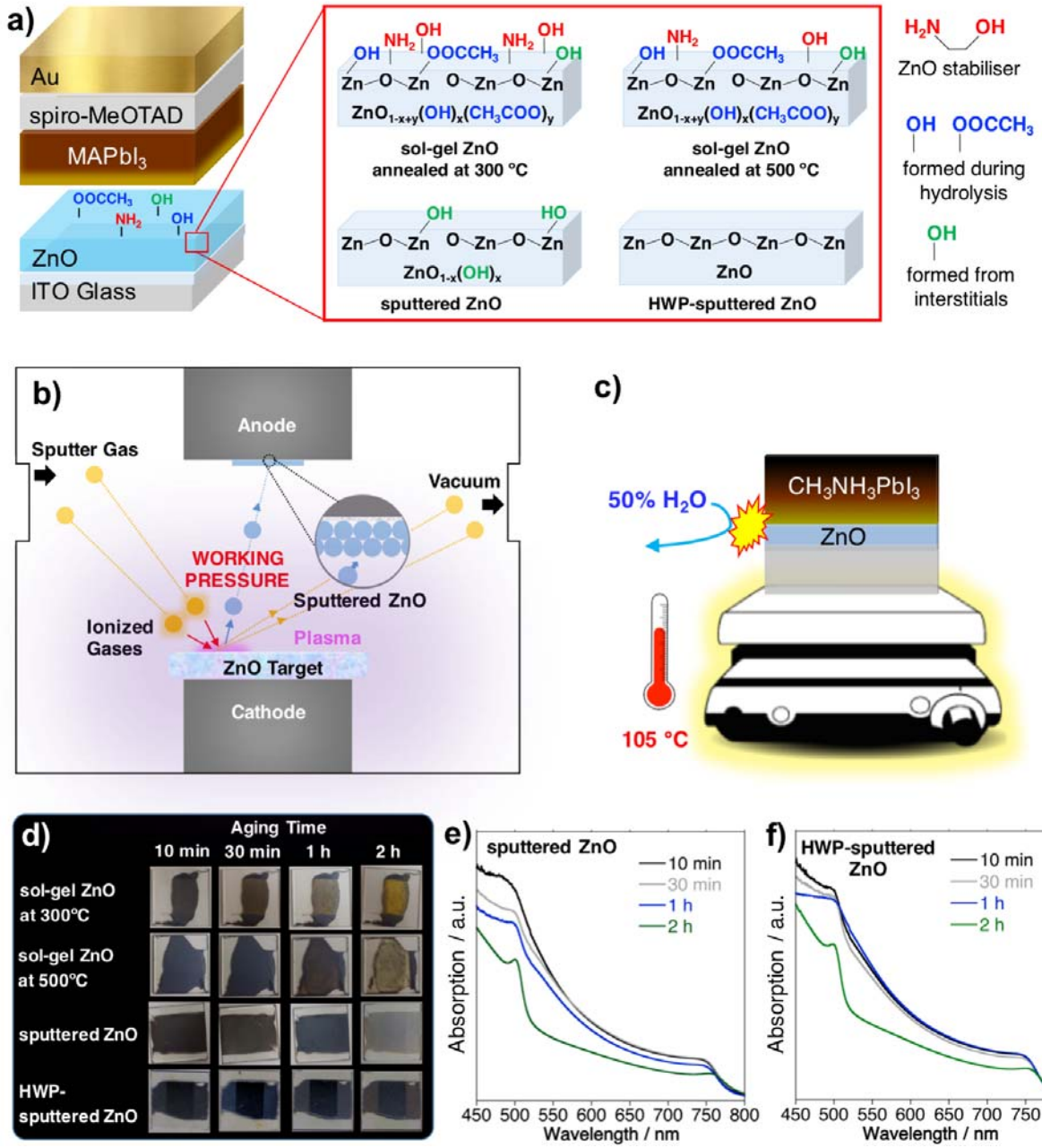

Figure 1. a) Structural schematics of a PSC using ZnO as ETL and four types of ZnO films with different surface properties. b) Graphical depiction of the inside of the sputtering chamber. c) Illustration of the aging process. d) Degradation images of perovskite films on different ZnO films during the aging process. UV–vis absorption spectra of the perovskite films on e) sputtered ZnO and f) HWP-sputtered ZnO during the aging process.

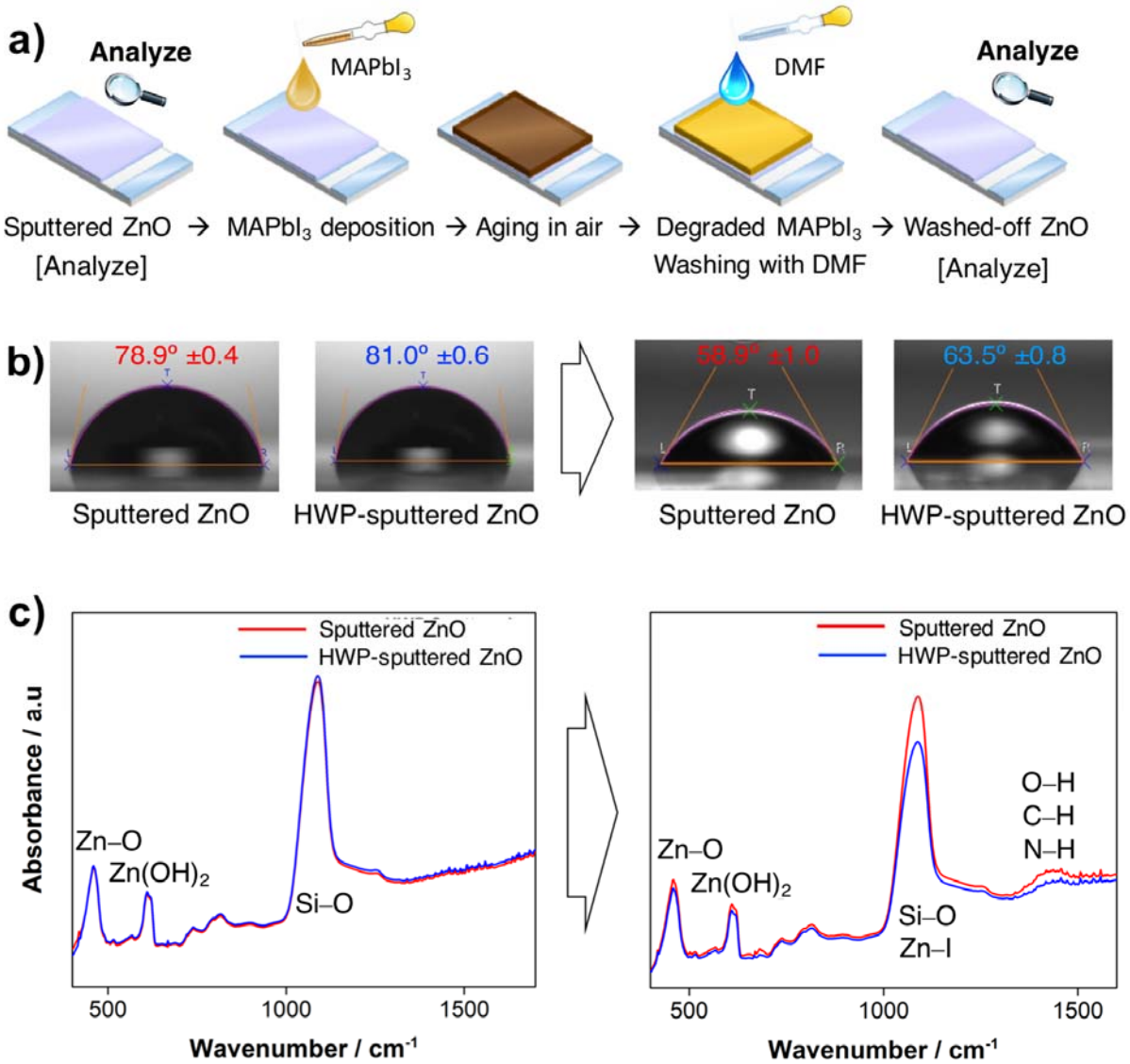

Figure 2. a) Illustration of analysis before and after the deposition and washing off $MAPbI_3$ from ZnO. b) Water contact angles of sputtered ZnO (red) and HWP-sputtered ZnO (blue) before (left) and after (right) the interaction of ZnO with $MAPbI_3$. c) FTIR data of sputtered ZnO (red) and HWP-sputtered ZnO (blue) before (left) and after (right) the interaction of ZnO with $MAPbI_3$.

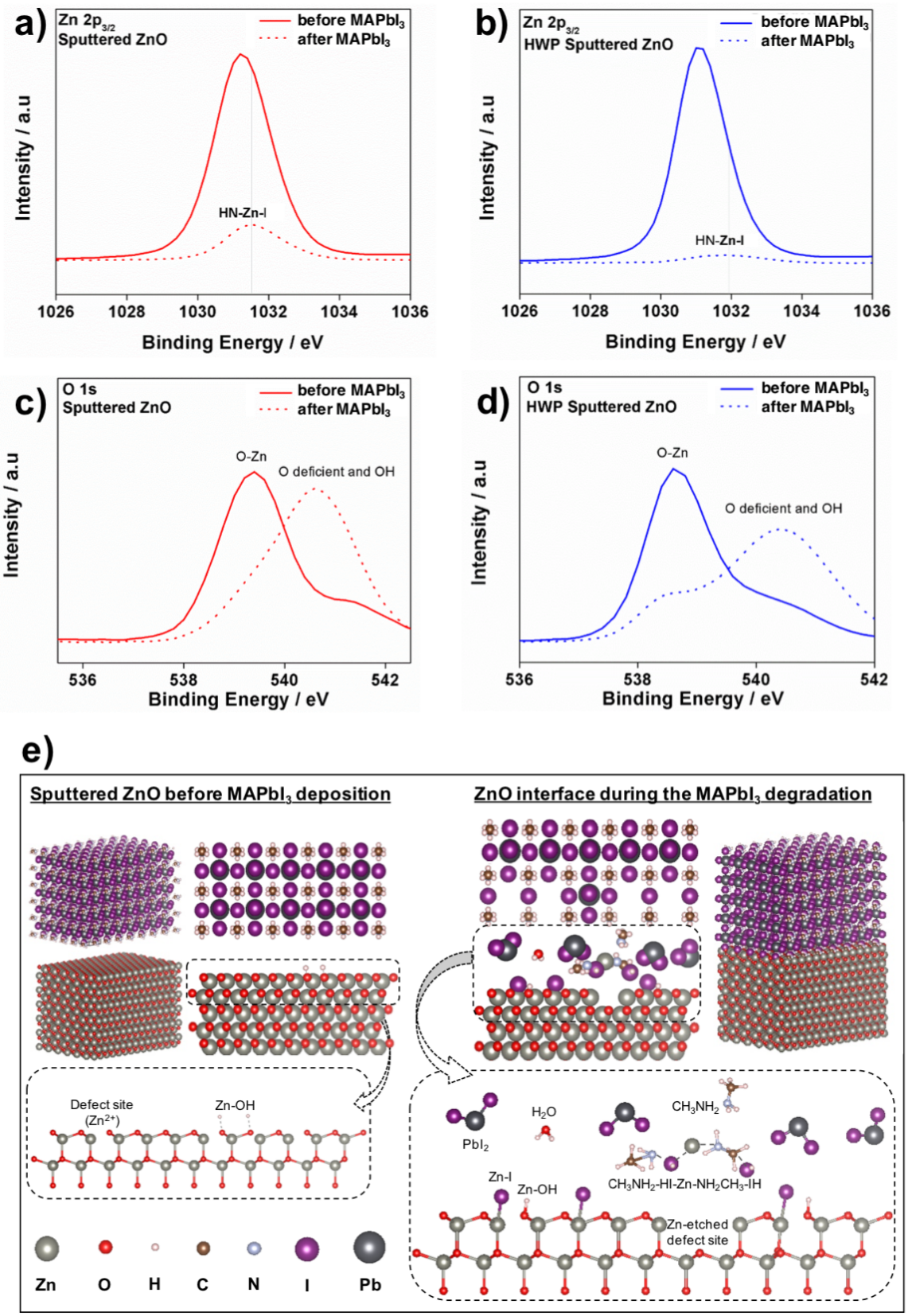

Figure 3. XPS Zn $2p_{3/2}$ peaks of a) conventionally sputtered ZnO and b) HWP-sputtered ZnO before (solid line) and after (dotted line) the interaction of ZnO with $MAPbI_3$. XPS O 1s peaks of c) conventionally sputtered ZnO and d) HWP-sputtered ZnO before (solid line) and after (dotted line) the interaction of ZnO with $MAPbI_3$. e) Graphical illustration of the interaction of ZnO with $MAPbI_3$ before the contact (left) and during the degradation (right). Vesta™ was used for the illustration.

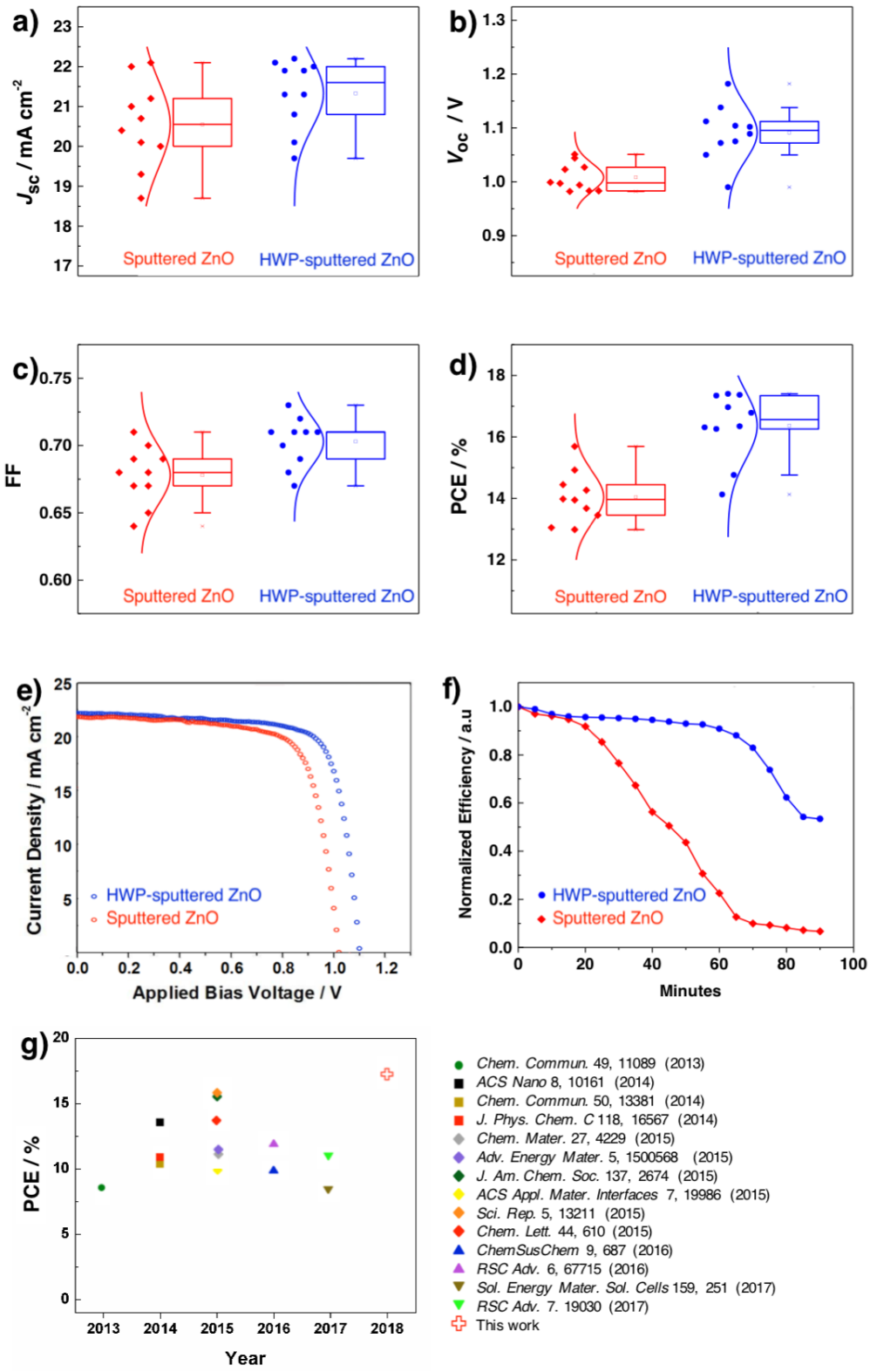

Figure 4. Statistical analysis of the sputtered ZnO ETL-based PSCs (red diamonds) and the HWP-sputtered ZnO ETL-based PSCs (blue squares) illustrating a) J_{SC}, b) V_{OC}, c) FF, and d) PCE distribution. e) *J–V* curves under forward bias of PSCs using a sputtered ZnO (red circles) and HWP-sputtered ZnO (blue circles). f) Stability test result of unencapsulated PSCs using a sputtered ZnO (red diamonds) and HWP-sputtered ZnO (blue squares) under constant illumination in air (20 °C, 30%). g) PCE record chart listing single compact ZnO layer-based PSCs reported thus far, including this work.

High-performance and stable ZnO-based perovskite solar cells are fabricated using sputtering process under high working pressure. Although ZnO is a good electron-transporting layer, its interaction with perovskite limits its application in perovskite solar cells. However, in this work, ZnO films with a good stoichiometry and minimum defects were produced using high-working-pressure sputtering, which results in a record-high performance of perovskite solar cells with high stability among the reported ZnO-based perovskite solar cells.

Keyword: ZnO, perovskite solar cells, sputtering, metal oxide surface, organic solar cells

I. Jeon, A. Thote, H.-S. Lin, S. Manzhos, T. Nakagawa, D. Suh, J. Hwang, M. Kashiwagi, J. Shiomi, S. Maruyama, H. Daiguji, Y. Matsuo

High-working-pressure Sputtering of ZnO for Stable and Efficient Perovskite Solar Cells

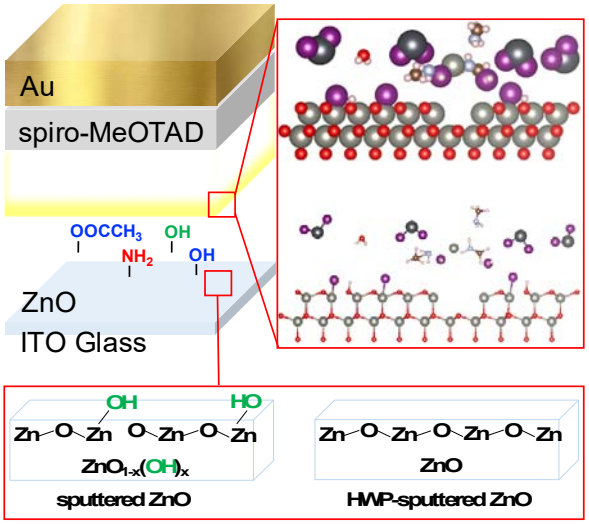

Supporting Information

High-working-pressure Sputtering of ZnO for Stable and Efficient Perovskite Solar Cells

Abhishek Thote,[†] Il Jeon,[†]* Hao-Sheng Lin,[†] Sergei Manzhos,[‡] Takafumi Nakagawa,[†] Donguk Suh,[†] Junho Hwang,[†] Makoto Kashiwagi,[†] Junichiro Shiomi,[†] Shigeo Maruyama,[†,§]* Hirofumi Daiguji[†]* and Yutaka Matsuo[†,⊥]*

† Department of Mechanical Engineering, The University of Tokyo 7-3-1 Hongo, Bunkyo-ku, Tokyo 113-8656, Japan

‡ Department of Mechanical Engineering, National University of Singapore, Block EA #07-08, 9 Engineering Drive 1, Singapore 117576, Singapore

§ Research Institute for Energy Conservation, National Institute of Advanced Industrial Science and Technology, Tsukuba 305-8565, Japan

⊥ Hefei National Laboratory for Physical Sciences at the Microscale, University of Science and Technology of China, Hefei, Anhui 230026, China

Corresponding Author

*E-mail: il.jeon@spc.oxon.org (I.J), E-mail: maruyama@photon.t.u-tokyo.ac.jp (S.M), E-mail: daiguji@thml.t.u-tokyo.ac.jp (H.D), E-mail: matsuo@photon.t.u-tokyo.ac.jp (Y.M)

ESI Contents

1. HWP Sputtering Illustration

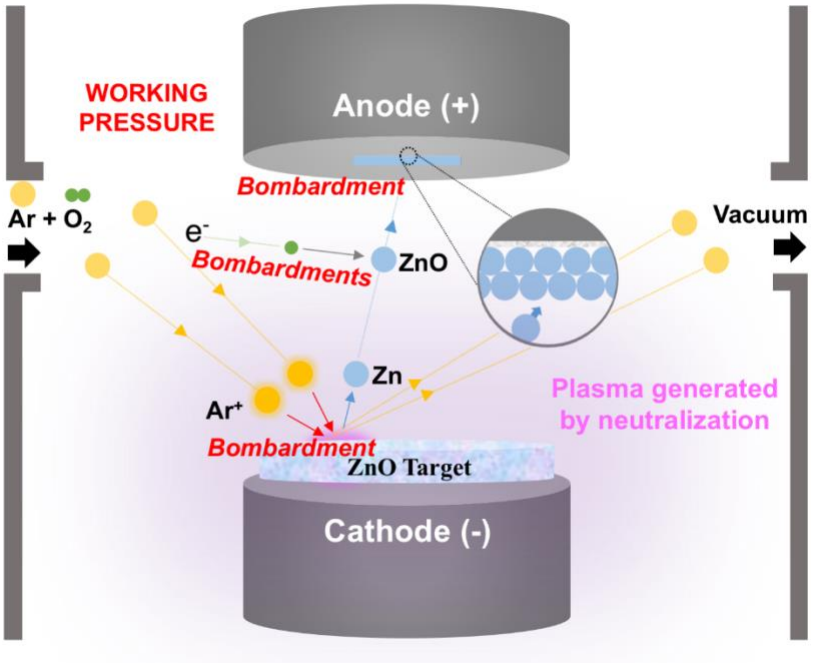

Figure S1 Illustration of the sputter chamber and locations of bombardment during the sputtering process

2. Pre-Annealing of ZnO

Table S1 PCE of PSCs using ZnO as the ETL before and after the pre-annealing treatment under 1 sun (AM 1.5 G, 100 mW cm^{-2}).

ETL	$PCE_{forward}$ (%)	
	Before 10 min pre-annealing	After 10 min pre-annealing
Sol-gel ZnO annealed at 300 ºC	3.9	7.65
Sol-gel ZnO annealed at 500 ºC	6.6	12.3
Sputtered ZnO	11.1	15.7
HWP-sputtered ZnO	12.3	17.4

3. EDX Analysis

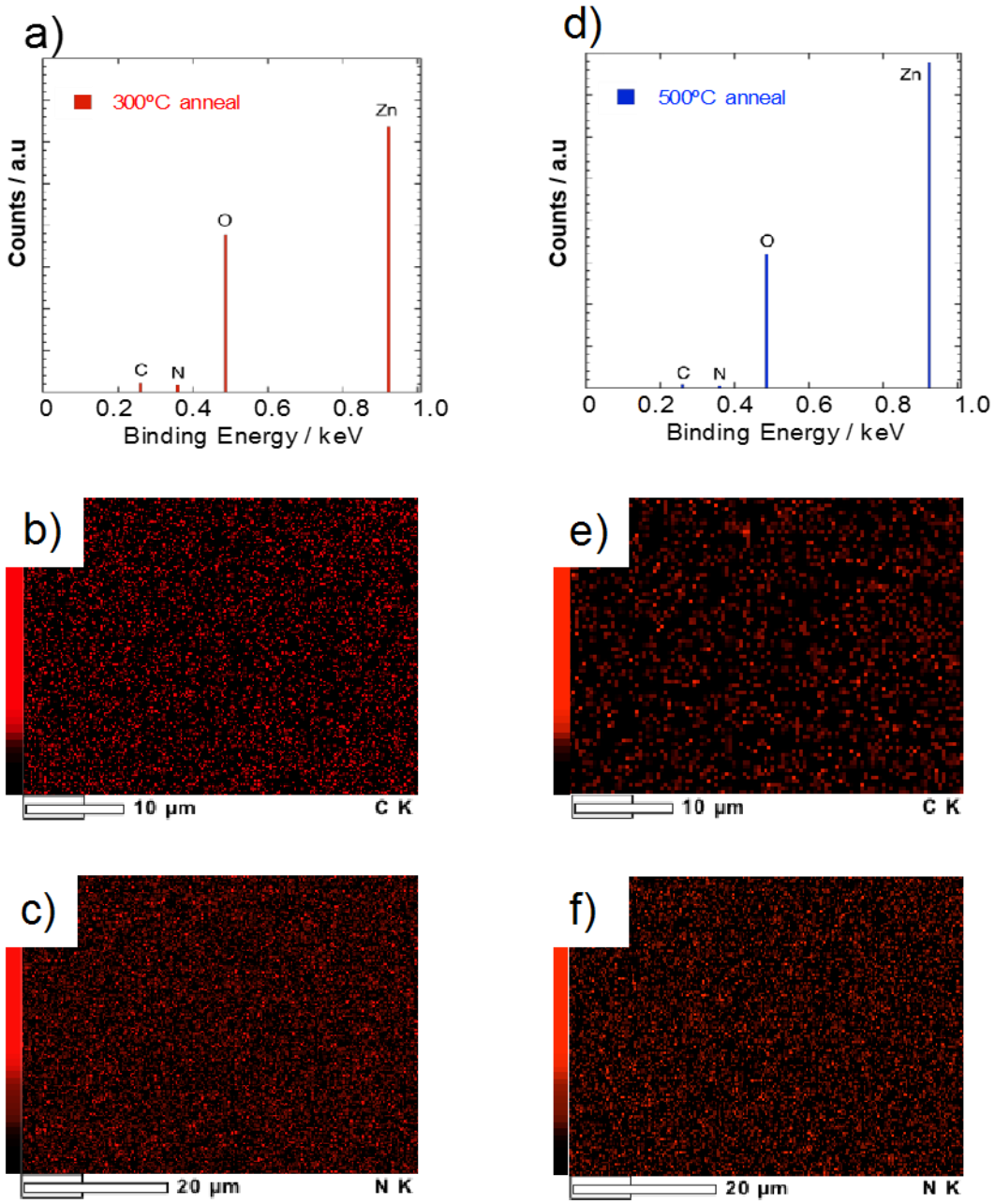

Figure S2 EDX analyses of ZnO films annealed at 300 °C: a) the spectra scan, b) carbon content mapping, and c) nitrogen content mapping; ZnO films annealed at 500 °C: d) the atomic weight scan, e) carbon content mapping, and f) nitrogen content mapping.

4. XPS Analysis 1

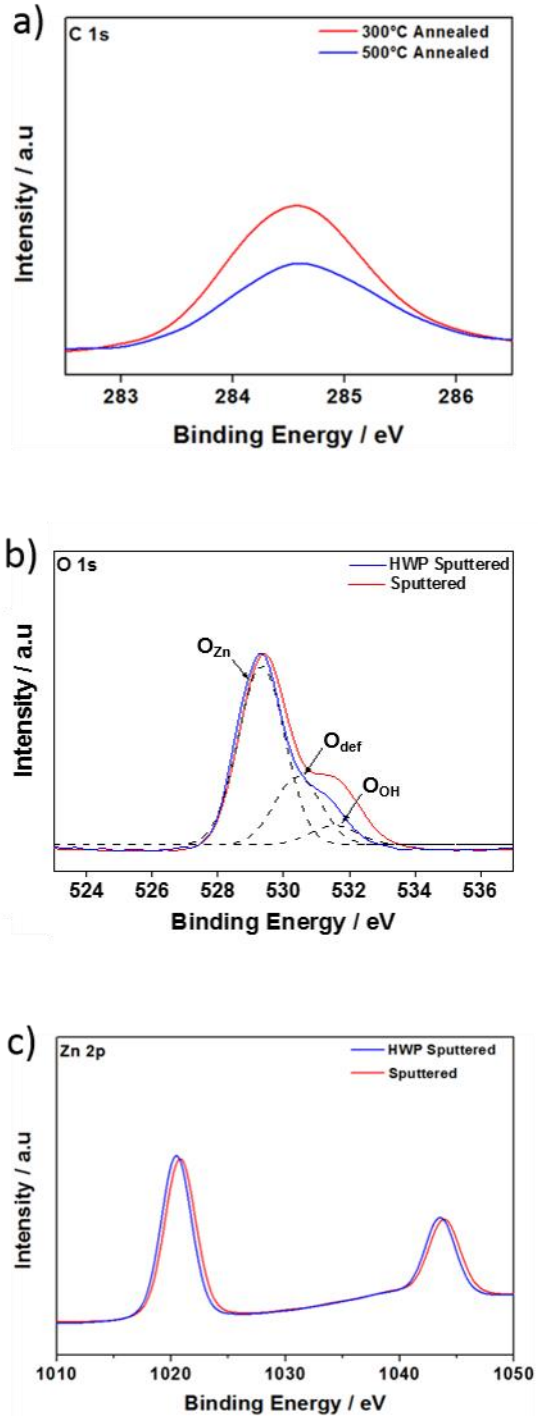

Figure S3 a) XPS carbon peaks of ZnO films annealed at 300 °C (red line) and 500 °C (blue line). XPS data comparison between HWP-sputtered ZnO (blue) and sputtered ZnO (red) for b) the O 1s peaks and c) the Zn $2p_{3/2}$ peaks.

5. PYS Analysis

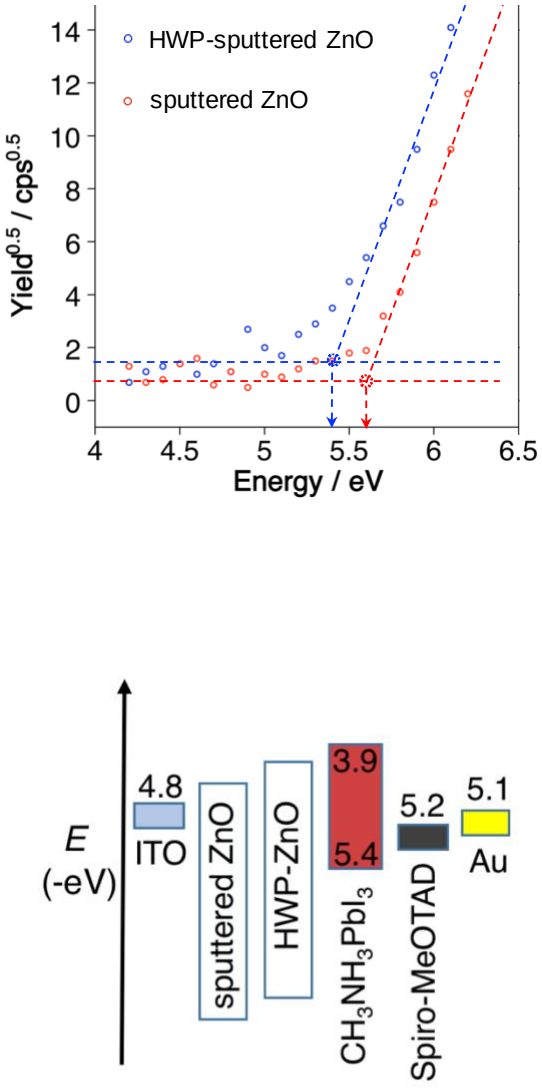

Figure S4 PYS data of HWP-sputtered ZnO (blue dots) and sputtered ZnO (red dots) (above), and energy level diagram with two different types of sputtered ZnO: conventionally sputtered and HWP-sputtered in PSCs (below).

6. XPS Analysis 2

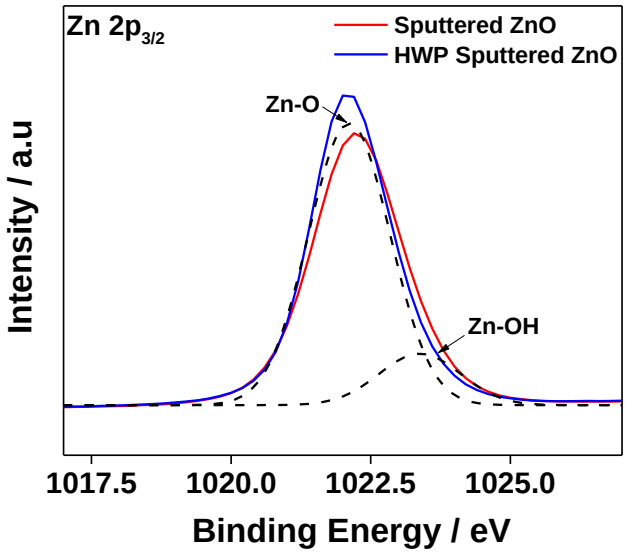

Figure S5 Zn $2p_{3/2}$ XPS peaks of sputtered ZnO (red) and HWP-sputtered ZnO (blue) overlapped at high resolution for better comparison

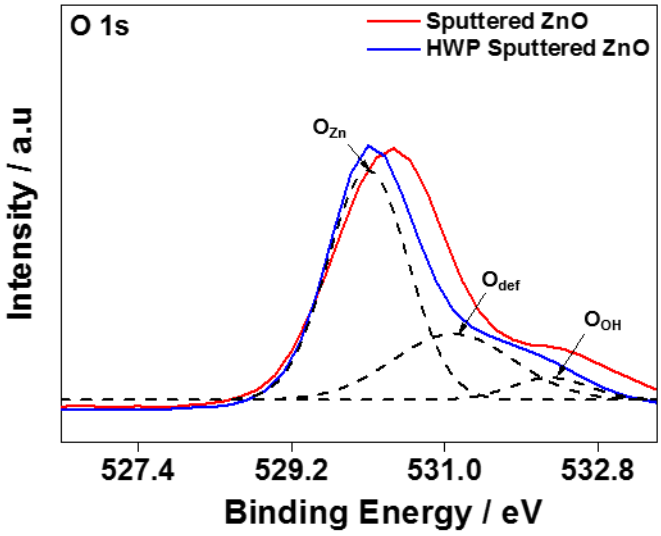

Figure S6 O 1s XPS peaks of sputtered ZnO (red) and HWP-sputtered ZnO (blue) overlapped at high resolution for better comparison

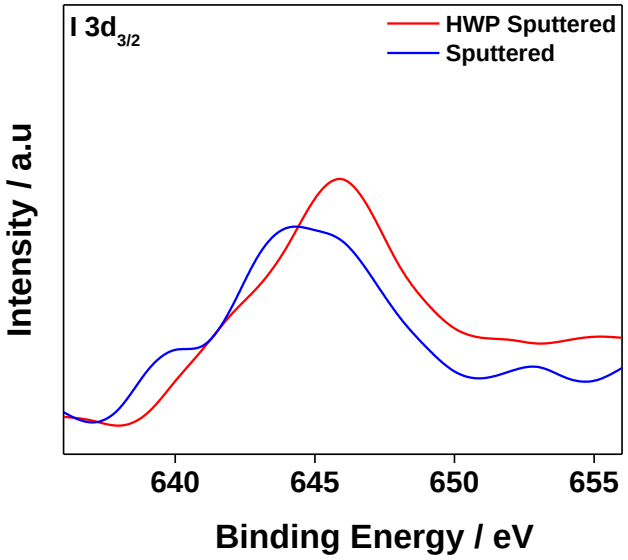

Figure S7 XPS data comparison between HWP-sputtered ZnO (blue) and sputtered ZnO (red) for I $3d_{3/2}$ peaks after the interaction of ZnO and $MAPbI_3$

7. Photoluminescence

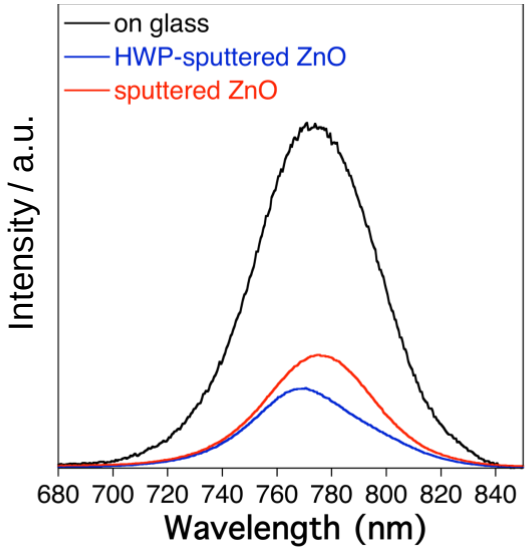

Figure S8 PL spectra of $CH_3NH_3PbI_3$ on glass (black line), on HWP-sputtered ZnO (blue line), and on sputtered ZnO (red line)

8. SEM analysis

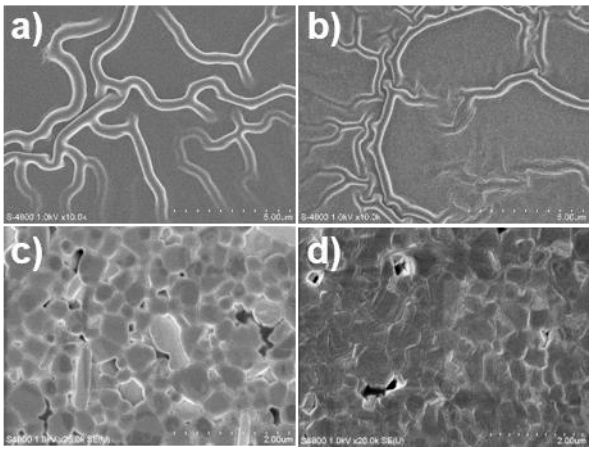

Figure S9 SEM images of sol-gel ZnO a) annealed at 300 °C, b) annealed at 500 °C, and $CH_3NH_3PbI_3$ on sol-gel ZnO c) annealed at 300 °C, d) annealed at 500 °C.

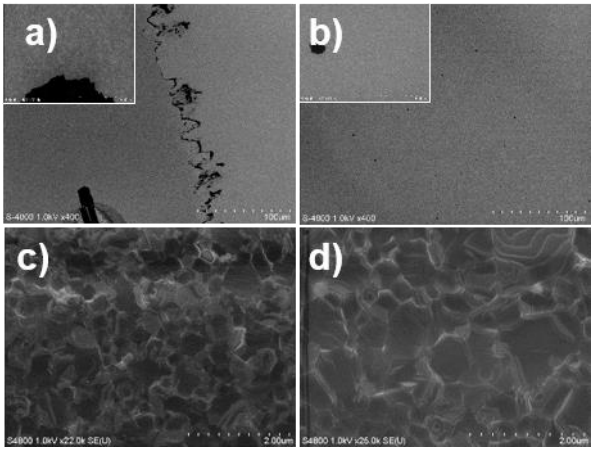

Figure S10 SEM images of a) sputtered ZnO, b) HWP-sputtered ZnO, and $CH_3NH_3PbI_3$ on c) sputtered ZnO, d) HWP-sputtered ZnO.

9. Photovoltaic Table

Table S2 Photovoltaic performance of PSCs using four different types of ZnO as the ETL under 1 sun (AM 1.5 G, 100 mW cm^{-2}). The PCE values are the best values with averages and error ranges in parentheses.

ETL	J_{SC} (mA cm^{-2})	V_{OC} (V)	FF	PCE_{best} (%) [average]	Hysteresis Index
Sol-gel ZnO annealed at 300 ºC	17.0	0.81	0.53	7.65 [5.47 ±0.89]	0.718
Sol-gel ZnO annealed at 500 ºC	19.9	0.93	0.60	12.3 [10.1 ±0.9]	0.620
Sputtered ZnO	22.1	1.0	0.68	15.7 [14.0 ±0.8]	0.238
HWP-sputtered ZnO	22.2	1.1	0.71	17.4 [16.4 ±1.1]	0.181